Generating Swing-Suppressed Maneuvers for Crane Systems with Rate Saturation

Michael J. Agostini, Gordon G. Parker, Hanspeter Schaub, Kenneth Groom, Rush D. Robinett

***Abstract*— Off-line crane maneuvers, resulting in zero residual payload swing, have been explored previously using parameterized sets of basis functions. Assumptions usually included an ideal servo response and symmetric inputs. Non-symmetric maneuvers, in general, don't have closed form basis function solutions. Actuator dynamics further complicate maneuver generation by introducing non-linearities such as saturation. One way to circumvent saturation is to constrain crane operation below the saturation levels of the actuators. This limits the set of available maneuvers and can lead to slower, more costly crane operation. This work explores the effects of a common servo non-linearity, velocity saturation, on the swing-free maneuver generation process. A method is presented for maneuver generation that exploits speed saturation while still yielding near swing-free payload motion. An optimization code is used to generate basis function parameters where the cost function includes the speed saturation effects via a simulation of the payload dynamics. Experimental results using a 1/16th scale crane are presented to illustrate the method.**

***Index Terms*— vibration control, nonlinearities, velocity saturation, basis function, crane**

I. Introduction

CRANES are used throughout the transportation and construction industry ranging in application from light-duty, small motion lift-assistance to multiple ton, large motion payload placement seen in construction operations. Regardless of size, payload control is a key to personnel and equipment safety.

Several methods have been developed which are devoted to controlling pendulation in crane systems. Such methods can be grouped into the two general classes of operator-in-the-loop methods and off-line maneuver generation. Operator-in-the-loop methods include command shaping strategies such as those in Parker, et al. [1] and the input shaping work of Singer and Seering [2]. Off-line methods, more relevant to the current study, have been investigated by several authors.

Earlier authors considered several methods for controlling payload swing at the end of the maneuver. Sakawa and Nakazumi [3] proposed a method for swing control for rotary cranes which combined an open and closed loop controller. During the course of the maneuver, the system input was driven by a proposed set of basis functions. Near the end of the maneuver, a closed loop controller damped out swing. Vaha, et al. [4] considered command generation for a boom crane, with the goal of having zero residual swing. Bang-coast-bang acceleration profiles were explored in simulation without compensating for centripetal acceleration induced swing excitation. Although offering an improvement over arbitrary point-to-point operations, residual swing was present. Auernig and Troger [5] considered the time optimal and swing-free maneuver generation for an overhead gantry crane. Analytical and simulation results were presented for variable lift-line operations. Maneuvers were generated by solving the time optimal formulation using the Pontryagin maximum principle.

Later authors considered more complicated systems, but tended to avoid rate saturation. Hämäläinen, et al. [6] proposed swing-free and energy optimal maneuvers for an overhead gantry crane with fixed final time constraints. Simple actuator dynamics were considered, and the optimizer was constrained to avoid rate saturation. Noakes and Jansen [7] also investigated residual swing-free maneuvers for an overhead gantry crane. Bang-coast-bang basis functions were employed, assuming ideal actuator dynamics. Moustafa and Ebeid [8] investigated controlling swing on a two degree of freedom overhead gantry crane using controller feedback. Part of their goal was to control payload vibration during the entire maneuver, not just the residual swing at the end. This was accomplished by using state feedback to move the eigenvalues of the system such that swing could decay to zero. Blazicevic and Novakovic [9] considered a variety of velocity basis functions applied to a boom crane. Swing-free maneuvers were the goal, again with ideal actuator dynamics assumed. Souissi and Koivo [10] had a model of a rotary crane which included boom inertia, an approximate winch, and both radial and tangential sway. Their proposed control strategy consisted of a PID control loop on the servo system with a feedback system to control payload swing. Petterson and Robinett [11] used bang-coast-bang trajectories to control the vibration of a flexible rod. Gravity caused a dynamic coupling between the horizontal and vertical bending modes. The solution to the problem was to set the length of each pulse equal to the system's period of vibration.

This work explores some of the limitations of using off-line optimization methods for real systems. Cranes often suffer from low maximum velocity as well as large dead zone and response lags. Typically, crane operators will intentionally speed saturate during a maneuver so as to position a load as quickly as possible. Constraining operation below speed saturation when designing an off-line maneuver could result in maneuvers that are slower than what is possible. This limitation makes it impractical to directly employ the bang-coast-bang acceleration commands such as those used by Pet-

This work was supported by NSWC Carterock under contract 092960725-2

M. Agostini and G. Parker are affiliated with Michigan Technological University. E-mail: agostini@mtu.edu and ggparker@mtu.edu.

H. Schaub, K. Groom, and R. Robinett are affiliated with Sandia National Laboratories, Albuquerque, New Mexico. E-mail: hschaub@sandia.gov, kngroom@sandia.gov, and rdrobin@sandia.gov.

terson and Robinett [11], where sufficient actuation capability existed.

The main contribution of this work is a procedure for finding swing-free maneuvers while exploiting joint servo nonlinearities. This solution is based on the bang-coast-bang basis function method, but relaxes the constraints that the maneuver be symmetric. Unlike previous work in off-line command generation, the proposed approach permits fully coordinated multi-axis crane maneuvers. The optimization process used to generate the trajectory requires an accurate servo model capable of predicting the effects of servo nonlinearities on payload swing. The results show that the method is a viable alternative for designing trajectories for systems with nonlinear actuation, with particular emphasis given to systems with speed saturation.

Section II develops the crane payload dynamic model used for cost function evaluation. Section III presents the maneuver generation process, including the basis function parameterization and the simulation-based cost function. Section IV describes the experimental crane test bed and demonstrates the applicability of the approach through an example.

II. Payload Swing Dynamics

A crane system will be used as the test bed for the trajectory generation process. The position, rate, and acceleration of the crane axes are the inputs to the payload dynamic equations. Three kinematic relationships map the servo system rates into joint rates of the crane. The models for the three crane subsystems, payload dynamics, servo dynamics, and crane kinematics, are described in this section.

A. Payload Dynamics

The crane is shown in Figure 1 and has two revolute joints and one prismatic. The first revolute joint allows the tower and boom assembly to rotate about the $\hat{z}_I$ axis by an angle α. This motion is referred to as slew. The second revolute joint allows the boom to rotate by β about the $\hat{y}_s$ axis, and is called luff. The lift-line extension and retraction, called hoist and denoted as L_h, is the prismatic joint. The lift-line and payload assembly act as a spherical pendulum at the boom tip attachment point, resulting in two payload swing degrees-of-freedom. In the remainder of this section the full nonlinear payload swing dynamic equations are derived. To this end a detailed description of the coordinate frames is presented along with discussion about simulated versus measurable swing degrees-of-freedom.

The origin of the inertial frame, denoted $\{I\}$, lies along the slew axis at the point where the distance from the center of the boom pin to the slew axis is a minimum, as shown in Figure 1. The $\hat{z}_I$ axis points up. The slew frame, denoted $\{s\}$, is attached to the slewing tower and boom assembly with its origin coincident with $\{I\}$. The $\hat{z}_s$ axis lies along $\hat{z}_I$, the $\hat{x}_s$ axis remains directly below the boom such that when β is zero the boom lies on the $\hat{x}_s$ axis. The origin of the boom frame, denoted $\{b\}$ is at the center of the boom pin with its $\hat{x}_b$ axis along the boom. Axes $\hat{y}_I$, $\hat{y}_b$, and $\hat{y}_h$ are not explicitly shown

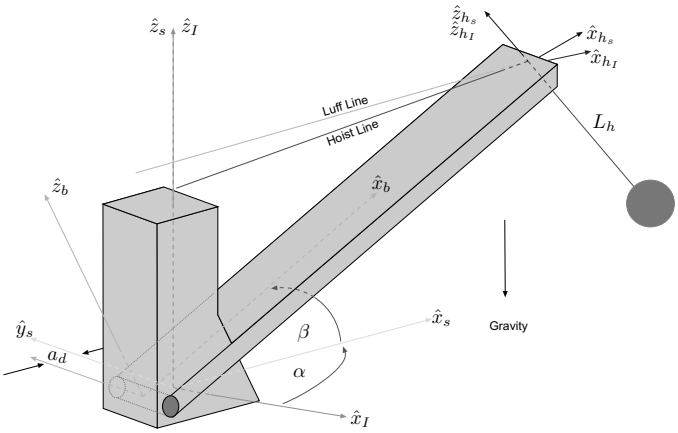

Fig. 1. Crane System

in Figure 1, but are defined such that the coordinate systems conform to right right-hand convention.

Two different sets of swing angles are used – one for simulation and one for comparison with measurements. For simulation purposes the swing angles are defined relative to the inertial frame using a rotation sequence of ρ about the negative $\hat{y}_I$ axis, then a rotation of τ about the new negative $\hat{x}$ axis. The resulting hoist frame is denoted $\{h_I\}$. The rotation matrix which transforms a vector represented in $\{h_I\}$ frame to $\{I\}$ is

$$ {}^{I}_{h_I}R = \begin{bmatrix} \cos\rho & 0 & \sin\rho \\ 0 & 1 & 0 \\ -\sin\rho & 0 & \cos\rho \end{bmatrix} \begin{bmatrix} 1 & 0 & 0 \\ 0 & \cos\tau & -\sin\tau \\ 0 & \sin\tau & \cos\tau \end{bmatrix} \quad (1) $$

where ρ and τ are the inertial radial and tangential swing angle degrees-of-freedom.

Swing measurements are made using a 2-axis potentiometer mounted at the boom tip. New swing degrees-of-freedom, denoted θ_r and θ_t, are defined relative to the $\{s\}$ frame, using the same Y-X rotation sequence. The resulting hoist frame is denoted $\{h_s\}$, where the rotation matrix that transforms a vector represented in the $\{h_s\}$ frame to the $\{s\}$ frame is

$$ {}^{s}_{h_s}R = \begin{bmatrix} \cos\theta_r & 0 & \sin\theta_r \\ 0 & 1 & 0 \\ -\sin\theta_r & 0 & \cos\theta_r \end{bmatrix} \begin{bmatrix} 1 & 0 & 0 \\ 0 & \cos\theta_t & -\sin\theta_t \\ 0 & \sin\theta_t & \cos\theta_t \end{bmatrix}. \quad (2) $$

Note $\hat{z}_{h_s}$ and $\hat{z}_{h_I}$ have the same orientation. The measured swing angles, θ_{t_m} and θ_{r_m} are simply

$$ \theta_{t_m} = \theta_t \quad (3) $$

$$ \theta_{r_m} = \theta_r - \beta \quad (4) $$

Since the simulation swing angles (ρ and τ) are different from the $\{s\}$ frame relative angles (θ_r and θ_t), a set of transformation equations is required so that θ_r and θ_t can be computed from simulation results and compared to measurements. The slew axis relative angles can be written in terms of the simulation swing angles by noting that

$$({}^{s}_{h_s}R - {}^{s}_{I}R \cdot {}^{I}_{h_I}R) \cdot {}^{s}\hat{z}_s = 0 \tag{5}$$

where ${}^{s}_{I}R$ is the rotation matrix that transforms a vector represented in $\{I\}$ to a representation in $\{s\}$ and is

$${}^{s}_{I}R = \begin{bmatrix} \cos\alpha & \sin\alpha & 0 \\ -\sin\alpha & \cos\alpha & 0 \\ 0 & 0 & 1 \end{bmatrix} \tag{6}$$

Substituting Equations 1, 2, and 6 into 5 yields the following transformation equations

$$\begin{aligned} \tan\theta_r &= \frac{\sin\alpha\sin\tau + \cos\alpha\sin\rho\cos\tau}{\cos\rho\cos\tau} \\ \tan\theta_t &= \frac{\cos\alpha\sin\tau - \sin\alpha\sin\rho\cos\tau}{\cos\rho\cos\tau}\cos\theta_r \end{aligned} \tag{7}$$

where the transformation equations must be evaluated in the order presented to accommodate the dependency of θ_t on θ_r.

The main reason for using the ρ and τ swing angles for simulation is that the swing dynamic equations can be written in a compact and computationally efficient form without any linearizing assumptions imposed. An outline of this procedure, with the resulting swing dynamic equations follows.

The vector from the origin of the inertial frame to the payload, represented in the inertial frame, is

$${}^{I}\vec{p}_p = {}^{I}\vec{p}_b + {}^{I}_{h_I}R\,{}^{h_I}\vec{P}_1 \tag{8}$$

where ${}^{I}\vec{p}_b$, the vector from the origin of $\{I\}$ out to the boom tip, represented in $\{I\}$, and is

$${}^{I}\vec{p}_b = \begin{Bmatrix} x \\ y \\ z \end{Bmatrix} = \begin{Bmatrix} -a_d\cos(\alpha) + L_b\cos(\alpha)\cos(\beta) \\ -a_d\sin(\alpha) + L_b\sin(\alpha)\cos(\beta) \\ L_b\sin(\beta) \end{Bmatrix} \tag{9}$$

and the vector ${}^{h_I}\vec{P}_1$ is from the origin of $\{h_I\}$ to the payload and is

$${}^{h_I}\vec{P}_1 = \begin{Bmatrix} 0 \\ 0 \\ -L_h \end{Bmatrix} \tag{10}$$

Forming the kinetic and potential energy, and then applying Lagrange's equations gives the full nonlinear swing dynamic equations

$$\begin{aligned} L_h\ddot{\tau} = \; & -2\dot{L}_h\dot{\tau} - L_h\dot{\rho}^2\cos\tau\sin\tau - g\cos\rho\sin\tau + \\ & \ddot{x}\sin\rho\sin\tau + \ddot{y}\cos\tau - \ddot{z}\cos\rho\sin\tau \end{aligned} \tag{11}$$

$$\begin{aligned} L_h\cos\tau^2\ddot{\rho} = \; & 2L_h\dot{\rho}\dot{\tau}\sin\tau\cos\tau - 2\dot{L}_h\dot{\rho}\cos\tau^2 - \\ g\sin\rho\cos\tau - \; & \ddot{x}\cos\rho - \ddot{z}\sin\rho\cos\tau \end{aligned} \tag{12}$$

where the boom tip accelerations, in terms of the slew and luff angles, are

$$\ddot{x} = a_d\left(\dot{\alpha}^2\cos\alpha - \ddot{\alpha}\sin\alpha\right) + L_b\big[2\dot{\alpha}\dot{\beta}\sin\alpha\sin\beta - \left(\dot{\alpha}^2 + \dot{\beta}^2\right)\cos\alpha\cos beta - \ddot{\alpha}\sin\alpha\cos\beta - \ddot{\beta}\cos\alpha\sin\beta\big] \tag{13}$$

$$\ddot{y} = a_d\left(\dot{\alpha}^2\sin\alpha - \ddot{\alpha}\cos\alpha\right) + L_b\big[-2\dot{\alpha}\dot{\beta}\cos\alpha\sin\beta - \left(\dot{\alpha}^2 + \dot{\beta}^2\right)\sin\alpha\cos beta + \ddot{\alpha}\cos\alpha\cos\beta - \ddot{\beta}\sin\alpha\sin\beta\big] \tag{14}$$

$$\ddot{z} = L_b\left(-\dot{\beta}^2\sin\beta + \ddot{\beta}\cos\beta\right) \tag{15}$$

The values of the test bed crane parameters used in the dynamic equations are provided in Table I.

TABLE I
CRANE PARAMETERS

Parameter	Units	Value
a_d	[m]	0.017
L_b	[m]	2.37
L_h	[m]	1.00

B. Servo Dynamics

The high-level commands to the crane are slew, luff, and hoist speeds. A set of kinematic relationships maps these commands into servo motor speed commands and a servo-loop converts them into motor currents that drive the hoist and luff winches, and the slew gear. In previous work on off-line maneuver generation these servo dynamics were assumed to be negligible. For small motions this may be appropriate; however, there will always be rate saturation when the commands are too large. The ability to exploit these high rates, and the general effect of servo dynamics on the maneuver generation process, is the focus of Section IV. This section describes two servo models used and introduces the terminology used to distinguish them.

The first servo model captures the bandwidth limitations and nonlinearities of the experimental crane test bed. The second model is simply a unity transfer function between commanded and realized joint rates. Most importantly for this study, it does not capture the speed saturation present in the real servo system. In the remainder of this document these two models are called the *nonlinear* and *ideal* servo models, respectively.

1) Nonlinear Servo Model: A generic block diagram of the nonlinear servo model for either slew, luff or hoist is shown in Figure 2. The parameter $\dot{\theta}_c$ is the commanded speed, V_b is a constant to account for motor amplifier bias and gravity effects in luff and hoist, $\dot{\theta}_m$ is the output motor speed, F_s is a nonlinear saturation function, F_{dz} is a nonlinear dead-zone function, V_m is the motor voltage, K_p, K_I and K_f are the servo controller gains, while K_m and τ_m are the motor/amplifier gain and time constant respectively.

The time-domain equations for the servo model, are

$$\left(K_p + K_f\right)\dot{\theta}_c - K_p\dot{\theta}_m + K_I\left(\theta_c - \theta_m\right) = V_i \tag{16}$$

$$V_o = F_s\left(V_i\right) \tag{17}$$

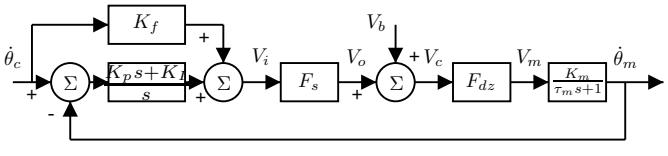

Fig. 2. Drive System Servo Model

$$V_c = V_o + V_b \tag{18}$$

$$V_m = F_{dz}\left(V_c\right) \tag{19}$$

$$\tau_m \ddot{\theta}_m + \dot{\theta}_m = K_m V_m \tag{20}$$

where the saturation function, F_s, is described by

$$V_o = \begin{cases} V_{o,max} & : & V_{o,max} & \leq & V_i & & \\ V_i & : & V_{o,min} & < & V_i & < & V_{o,max} \\ V_{o,min} & : & & & V_i & \leq & V_{o,min} \end{cases} \tag{21}$$

and F_{dz} is a nonlinear dead-zone function described by

$$V_m = \begin{cases} V_c - V_{dz} & : & V_{dz} & \leq & V_c & & \\ 0 & : & -V_{dz} & < & V_c & < & V_{dz} \\ V_c + V_{dz} & : & & & V_c & \leq & -V_{dz} \end{cases} \tag{22}$$

The values for the parameters K_p, K_I, V_b, K_m, and α_m, unique for each axis of the crane test bed, are listed in Table II.

TABLE II
NONLINEAR SERVO MODEL PARAMETERS FOR ALL 3 CRANE AXES.

Name	Units	Axis		
		Luff	Slew	Hoist
K_f	[volt/deg/sec]	0.0056	0.0053	0.0050
K_p	[volt/deg/sec]	0.02	0.05	0.02
K_I	[volt/deg]	0.025	0.005	0.025
$V_{o,min}$	[volt]	-11.3	-10	-10
$V_{o,max}$	[volt]	11.3	10	11
V_{dz}	[volt]	0	0.35	0
V_b	[volt]	-1.85	-0.33	0.50
K_m	[deg/sec/volt]	143	145	177
α_m	[1/sec]	100	100	100

The model was experimentally verified and accurately predicts unsaturated and saturated servo speed behavior with less than 3% error, where the error was defined as,

$$\%Error = \left| \frac{\dot{\theta}_{sim} - \dot{\theta}_{exp}}{\dot{\theta}_{exp}} \right| 100. \tag{23}$$

where $\dot{\theta}_{sim}$ and $\dot{\theta}_{exp}$ were simulated and experimental joint time histories.

2) Idealized Servo System: The ideal servo system is simply a unity transfer function between the commanded rates and the servo response.

$$\frac{\dot{\theta}_m}{\dot{\theta}_c} = 1 \tag{24}$$

This system is used in the trajectory generation process to illustrate the effects of neglecting actuator dynamics in systems dominated by them.

C. Crane Kinematics

The crane's slew, luff, and hoist joints are driven by DC motors, however, the crane axes are not connected directly to the motors. The slew axis to motor gear ratio is 1:120, resulting in proportional slew and slew motor rates

$$\dot{\alpha} = -\frac{\dot{\theta}_{m_s}}{120} \tag{25}$$

where $\dot{\theta}_{m_s}$ is the slew motor shaft rate.

Luff and hoist use a more complicated winch and cable system. A side-view of the crane cabling system is shown in Figure 3 to help illustrate the kinematic relationships described in the remainder of the section.

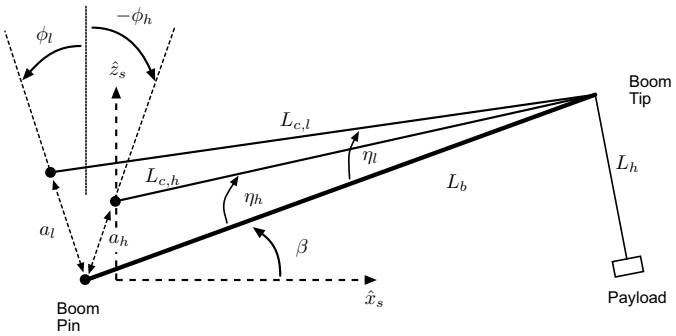

Fig. 3. Side-view of crane cabling to illustrate the parameters for relating hoist and luff rates to motor rates.

The luff rate, $\dot{\beta}$ is related to the luff motor rate, $\dot{\theta}_{m_l}$, by

$$\dot{\beta} = \left[\frac{5 a_l L_b \cos\left(\beta - \phi_l\right)}{r_l L_{c,l}} \dot{\theta}_{m_l} \right] \tag{26}$$

where r_l is the radius of the luff winch, a_l is the distance from the center of the boom pin to the center of the upper luff pulley, and ϕ_l is the angle between the slew axis and the line segment with length a_l. The varying quantity $L_{c,l}$ is the length of cable between the upper luff pulley and the boom tip, and is

$$L_{c,l} = \sqrt{a_l^2 + L_b^2 - 2 a_l L_b \sin\left(\beta - \phi_l\right)}. \tag{27}$$

The lift-line rate, $\dot{L}_h$ is a function of both the hoist motor rate $\dot{\theta}_{m_h}$ and the luff rate $\dot{\beta}$

$$\dot{L}_h = -\frac{r_h}{2} \dot{\theta}_{m_h} + 3 \frac{a_h L_b}{L_{c,h}} \cos\left(\beta - \phi_h\right) \dot{\beta} \tag{28}$$

where r_h is the radius of the hoist winch, $\dot{\theta}_{m_h}$ is the hoist motor shaft rate, a_h is the distance from the center of the boom pin to the center of the upper hoist pulley, and ϕ_h is the angle between the slew axis and the line segment with length a_h. The length of the cable between the upper hoist pulley and the boom tip, $L_{c,h}$, is

$$L_{c,h} = \sqrt{a_h^2 + L_b^2 - 2a_h L_b \sin(\beta - \phi_h)}. \qquad (29)$$

The values of the parameters used in Equation 26 through Equation 29 are provided in Table III for the crane test bed.

TABLE III
CRANE PARAMETERS

Parameter	Units	Value
r_{m_L}	[m]	0.0257
r_{m_h}	[m]	0.0257
a_{1_L}	[m]	0.703
a_{1_h}	[m]	0.660
ϕ_L	[rad]	0.0785
ϕ_h	[rad]	-0.0524
a_d	[m]	0.017
L_b	[m]	2.37
L_h	[m]	1.00

In the experiments in Section IV, the lift-line length, L_h, is held constant. From Equation 28 it should be noted that the hoist motor rate is not in general zero when $\dot{L}_h$ is zero. Therefore, even when the lift-line is held at a constant length the hoist servo dynamics can play a roll in the resulting payload motion.

III. AUTOMATED MANEUVER GENERATION

The maneuver time history for each crane axis is defined by a prescribed bang-coast-bang acceleration basis function. An optimization code chooses the parameters that define the maneuver such that the residual payload swing is minimized. The rest of this section describes the basis function design and optimization process.

A. Basis Function Design

The bang-coast-bang acceleration profile shown in Figure 4 is used as the basis function for the two crane axes ($\ddot{\beta}$ and $\ddot{\alpha}$). Of the parameters found in Table IV, t_{p_1}, t_{p_2} and t_f, are selected during the maneuver generation process. The final position p_δ is a constant throughout the maneuver generation process, having been chosen by an operator. The rest of the parameters are constrained by the three equations shown in Table V. Unlike previous work in off-line crane maneuver generation, no symmetry constraint is imposed on the acceleration profile.

The maneuvers are designed in the slew, luff, hoist crane joint space. For implementation, these joint velocities are converted into motor rates using the kinematic relationships of Equation 25 through Equation 29. Motor rates are then sent as inputs to the joint servos modeled by Equation 16 through Equation 22 for the nonlinear version and Equation 24 for the ideal version.

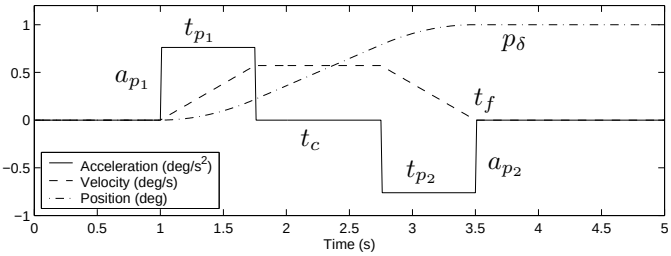

Fig. 4. Bang-Coast-Bang basis function

TABLE IV
BANG-COAST-BANG PARAMETERS

t_{p_1}	Duration of first acceleration pulse
t_{p_2}	Duration of second acceleration pulse
t_c	Duration of coast between acceleration pulses
t_f	Total duration of the command
a_{p_1}	Amplitude of first acceleration pulse
a_{p_2}	Amplitude of second acceleration pulse
p_δ	Resulting change in orientation

B. Optimization-Based Maneuver Generation

An optimization process is employed to select basis function parameters which minimize residual payload swing. It should be noted that the numerical optimization method is used to generate a feasible maneuver. It is not implied that the result is globally optimal, and it does not need to be in practice.

A dynamic simulation called CraneSim was written in C where payload swing was computed using the nonlinear dynamic equations described in Section II-A. The crane speed servos (on luff, slew, and hoist) are modeled as described in Section II-B. A software switch enables either the nonlinear servo system or the idealized servo system.

The external optimization was implemented using a sequential quadratic programming method. The optimization variables were the six independent time quantities t_f, t_{p_1}, and t_{p_2} for both the slew and luff trajectories. The final time was constrained such that $t_f + 0.05 > t_{p_1} + t_{p_2}$ for the slew and luff axes. Pulse amplitudes, used to drive the simulation, were computed from the equations in Table V.

The cost function of Equation 30 was used to penalize swing after the repositioning maneuver completed at $t = t_f$.

$$\Gamma = \int_{t_f}^{4T} \sqrt{\theta_r^2 + \theta_t^2}\, \mathrm{d}t \qquad (30)$$

TABLE V
CONSTRAINT EQUATIONS

	Luff Axis
Time	$t_f = t_{p_1} + t_{p_2} + t_c$
Position	$p_\delta = a_{p_1} t_{p_1} \left(\frac{1}{2} t_{p_1} + \frac{1}{2} t_{p_2} + t_c\right)$
Acceleration	$t_{p_1}\ a_{p_1} = t_{p_2}\ a_{p_2}$
	Slew Axis
Time	$t_f = t_{p_1} + t_{p_2} + t_c$
Position	$p_\delta = a_{p_1} t_{p_1} \left(\frac{1}{2} t_{p_1} + \frac{1}{2} t_{p_2} + t_c\right)$
Acceleration	$t_{p_1}\ a_{p_1} = t_{p_2}\ a_{p_2}$

Integration of residual swing begins at the end of the maneuver and lasts for 4 periods, T,

$$T = 2\pi\sqrt{\frac{L_h}{g}} \tag{31}$$

thus penalizing residual swing without penalizing swing during the course of the maneuver.

The optimization for each data set required approximately 15 minutes on a Sun Ultra-80 with two 450MHz UltraSPARC-II processors.

IV. Experimental Results

A 1/16th scale version of the TG3637 ship crane, used by the U.S. Navy, was used for the experimental verification of the maneuver generation approach. In general, this method allows the full operating regime of the crane to be exploited, including joint rate saturation, acceleration saturation, or deadzone. The experiments presented here focus on the rate saturation nonlinearity since it is one of the most limiting in real crane operations.

Two different maneuvers were considered, one sufficiently slow such that no joints reached rate saturation, the other faster allowing rate saturation.

The four combinations are summarized as

1) Non-saturating maneuver, ideal servo model during optimization
2) Non-saturating maneuver, nonlinear servo model during optimization
3) Saturating maneuver, ideal servo model during optimization
4) Saturating maneuver, nonlinear servo model during optimization

Both simulation and experimental results are presented for all four cases. Swing comparisons are made to assess the impact of including the nonlinear servo model into the maneuver generation process.

The encoder data was converted into acceleration by use of the second order differentiation filter,

$$\frac{\ddot{\theta}_{est}}{\theta_{enc}} = \frac{\omega_n^2 s^2}{s^2 + 2\zeta\omega_n s + \omega_n^2} \tag{32}$$

where $\omega_n = 20$, $\zeta = 0.8$, θ_{enc} is the encoder data, and $\ddot{\theta}_{est}$ is the estimated acceleration. The servo input was a velocity signal. For comparison with the output it was first integrated to position before being converted to and then passing the commanded positions through the same second order differentiation filter.

This filter mitigates high frequency noise inherent in the differentiation of encoder signals and tends to round-off the otherwise sharp transitions on the leading and trailing edges of the pulses.

A. Point-To-Point Maneuver Description

A coordinated maneuver was selected to test the effect of saturation. The test case consisted of lowering the boom from 65 to 35 degrees (β) while simultaneously slewing from 0 to 40 degrees (α). The hoist cable length was held to $1.0m$ which required a non-zero hoist motor rate as described in Section II-C. To quantify the amount of residual swing suppression, the magnitude of the residual swing was tabulated.

Swing was measured using two potentiometer-based swing sensor located at the boom-tip of the crane. The tangential swing used a linear potentiometer and the radial swing used a lower quality radial potentiometer. This resulted in more noise on the radial swing measurements. Voltages were converted into swing angles using a Chebyshev polynomial with coefficients obtained from a manual calibration over a range of 0 to 60 degrees. The calibration was accurate when interpolating, however, it was in error when extrapolating beyond 60 degrees. Since the maneuver in the experiments started at 65 degrees, there was approximately 0.5 degree error until the boom reached the calibration range, below 60 degrees.

B. Non-Saturating Maneuver Results

Here the nominal repositioning task was permitted to take up to 5.8 seconds. This resulted in joint rate commands that were below the saturation levels. Separate command histories were generated using both the ideal and nonlinear servo models defined by the basis function parameters shown in Table VI.

TABLE VI
BASIS FUNCTION PARAMETERS FROM OPTIMIZATION PROCESS FOR NON-SATURATED MANEUVERS

Optimized using Ideal Actuator Dynamics			
		Slew	Luff
t_{p_1}	[sec]	3.19	2.84
t_{p_2}	[sec]	1.93	1.46
t_{fp}	[sec]	5.88	5.31
Optimized using Nonlinear Actuator Dynamics			
t_{p_1}	[sec]	3.46	2.39
t_{p_2}	[sec]	1.99	1.69
t_{fp}	[sec]	5.78	5.36

The joint accelerations are shown in Figures 5 and 6, and the corresponding payload swing in Figures 7 and 8. Note that the commanded accelerations are different but the actual accelerations and resulting swing are nearly identical. For example, in Figure 5 the second slew acceleration pulse command begins at 4.25 seconds as does the actual acceleration. In contrast, in Figure 6 the second slew acceleration pulse command begins at 4.15 seconds, but the system doesn't respond until approximately 4.25 seconds. Although the commands are different, the crane responds the same, thus the payload swing of Figures 7 and 8, and summarized in Table VII, is nearly identical. The differences between the tangential and radial error for the two optimizations are at the noise level. This indicates, as expected, that assuming an ideal joint servo model is appropriate when the maneuver is sufficiently constrained to avoid servo speed saturation.

C. Saturating Maneuver Results

As in the previous section, two maneuvers were generated. One using the ideal joint servo model during the optimization

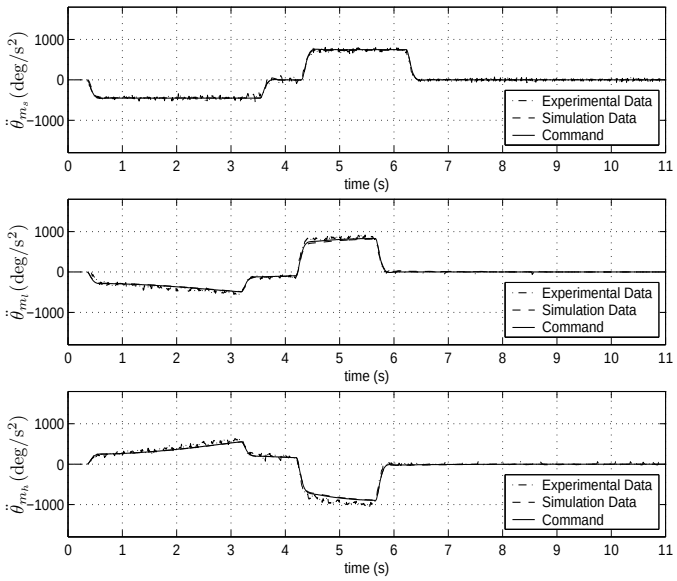

Fig. 5. Servo accelerations where the maneuver parameters were found assuming ideal actuator dynamics, but tested in a simulation where the joint dynamics were modeled. Joint rates were not allowed to saturate.

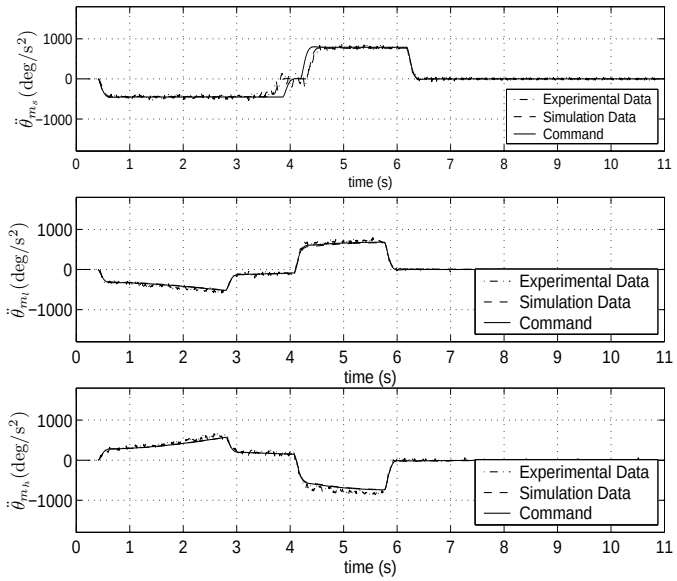

Fig. 6. Servo accelerations where the maneuver parameters were found using a simulation that included the actuator dynamics. Joint rates were not allowed to saturate.

TABLE VII

RESIDUAL SWING ERROR MAGNITUDES FOR THE NON-SATURATED MANEUVERS.

Optimized using Ideal Actuator Dynamics		
Tangential Error	[deg]	0.45
Radial Error	[deg]	0.70
Optimized using Nonlinear Actuator Dynamics		
Tangential Error	[deg]	0.55
Radial Error	[deg]	0.60

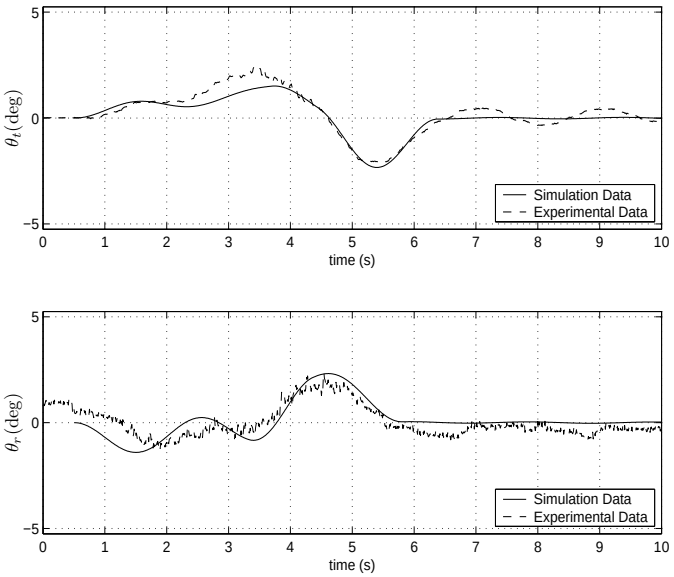

Fig. 7. Swing angles where the maneuver parameters were found assuming ideal actuator dynamics, but tested in a simulation where the joint dynamics were modeled. Joint rates were not allowed to saturate.

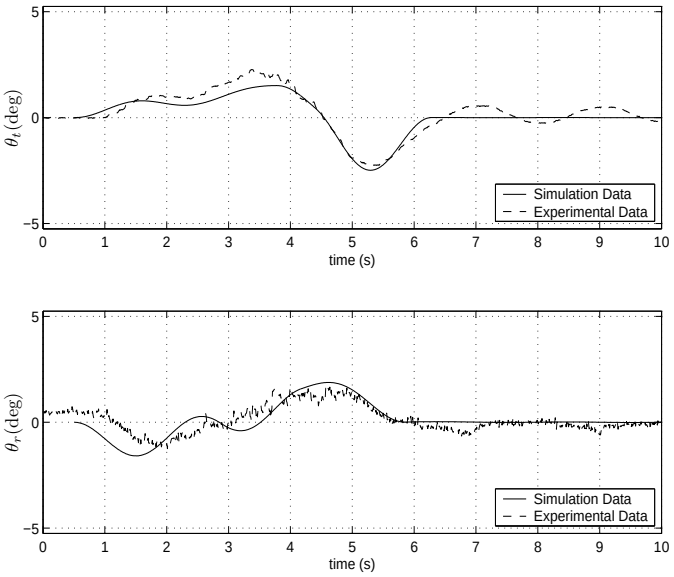

Fig. 8. Swing angles where the maneuver parameters were found using a simulation that included the actuator dynamics. Joint rates were not allowed to saturate.

process, the other using the nonlinear servo model. This time, joint rate commands were unconstrained, and allowed to saturate resulting in shorter duration maneuvers. The basis function parameters for both maneuvers are shown in Table VIII. As in the unsaturated maneuvers of Section IV-B, total maneuver time for the slew axis is nearly identical regardless of which servo model is employed. However, the luff axis command is 14% faster when the servo saturation was utilized by the maneuver.

The velocity saturation affects the width of the servo accelerations as illustrated in Figure 9. Note the width of the first pulse is truncated on the trailing edge and the width of the second pulse is truncated on the leading edge. In the following

TABLE VIII

BASIS FUNCTION PARAMETERS FROM OPTIMIZATION PROCESS FOR SATURATED MANEUVERS

Optimized using Ideal Actuator Dynamics			
		Slew	Luff
t_{p_1}	[sec]	1.67	1.84
t_{p_2}	[sec]	1.92	1.68
t_{fp}	[sec]	4.56	4.04
Optimized using Nonlinear Actuator Dynamics			
		Slew	Luff
t_{p_1}	[sec]	1.73	1.59
t_{p_2}	[sec]	2.58	1.28
t_{fp}	[sec]	4.66	3.47

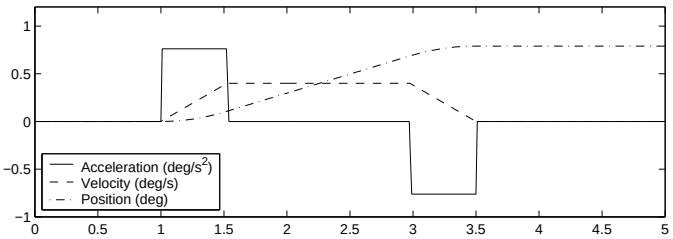

Fig. 9. Illustration of the effects of a 0.4 deg/s velocity saturation on the basis function shown in Figure 4.

results, this effect is most noticeable on the slew axis.

The servo accelerations shown in Figures 10 and 11 have similar pulse widths and amplitudes during the first pulse, but have quite different second pulse attributes. In particular, Figure 11 has a shorter duration but higher amplitude luff acceleration while Figure 11 has a shorter duration but higher slew acceleration. The ability of the maneuver to exploit the luff servo saturation is clearly evident when comparing the commanded accelerations of Figure 10 and Figure 11. When the servo model is assumed to be ideal, the command leads the actual luff acceleration by 0.3 seconds as seen in Figure 10. However, Figure 11 shows the command leading the actual acceleration by 0.7 seconds, thus anticipating the saturation and exploiting it sooner. Also, the simulated luff accelerations of Figure 11 perform much better in predicting the actual accelerations, again impacting the performance of the maneuver and its ability to reduce residual payload swing.

Figure 12 and Figure 13 show the payload swing for these two maneuvers, and Table IX summarizes the residual swing performance. The residual swing of Figure 13 is 4.5 times smaller than that of Figure 12, again illustrating the ability of the maneuver generation process to successfully exploit the servo saturation.

Table X shows the commanded and final luff and slew angles. There is a consistent 4% error between the commanded and actual final luff position across all the maneuvers. This is most likely attributed to servo model errors used during the maneuver generation. The slew axis final position error is about 2% for non-saturating maneuvers, and 5% for saturating maneuvers. This is an artifact of the optimization-based maneuver generation process. In general, there were

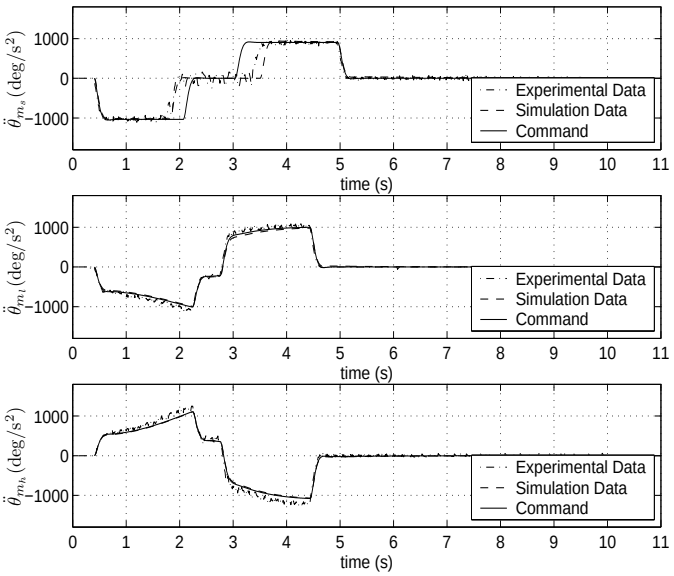

Fig. 10. Servo accelerations where the maneuver parameters were found assuming ideal actuator dynamics, but tested in a simulation where the joint dynamics were modeled. Joint rates were allowed to take on any value.

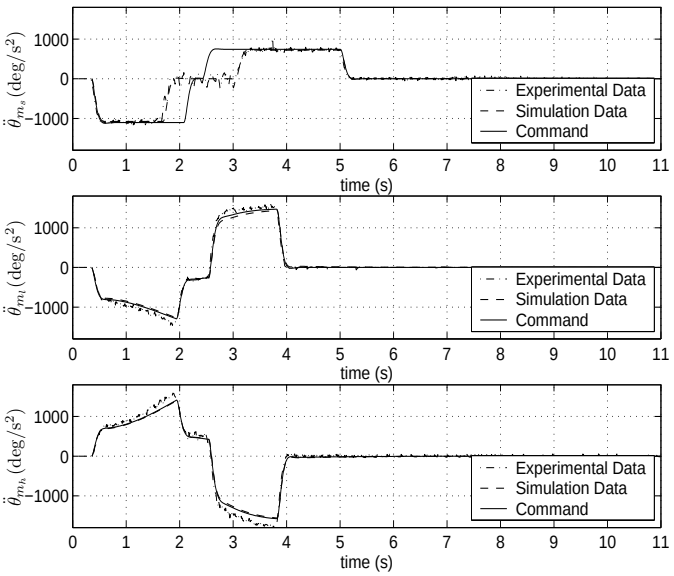

Fig. 11. Servo accelerations where the maneuver parameters were found using a simulation that included the actuator dynamics. Joint rates were allowed to take on any value.

TABLE IX

RESIDUAL SWING ERROR MAGNITUDES FOR THE SATURATED MANEUVERS.

Optimized using Ideal Actuator Dynamics		
Tangential Error	[deg]	2.28
Radial Error	[deg]	1.10
Optimized using Nonlinear Actuator Dynamics		
Tangential Error	[deg]	0.50
Radial Error	[deg]	0.65

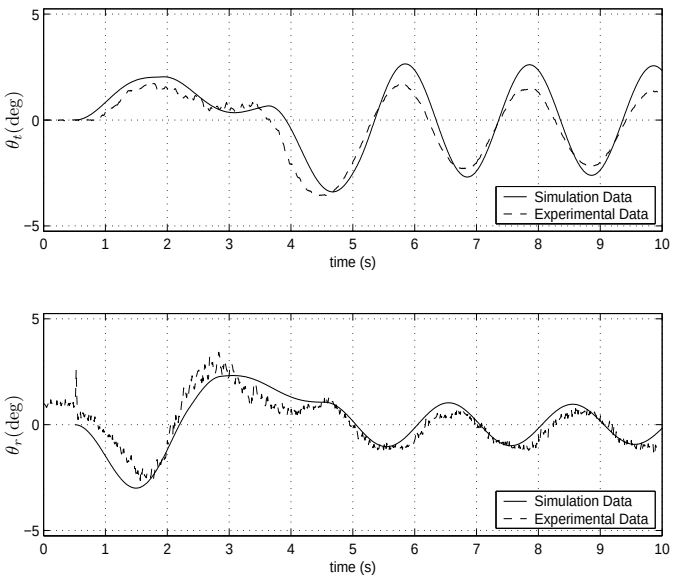

Fig. 12. Swing angles where the maneuver parameters were found assuming ideal actuator dynamics, but tested in a simulation where the joint dynamics were modeled. Joint rates were allowed to take on any value.

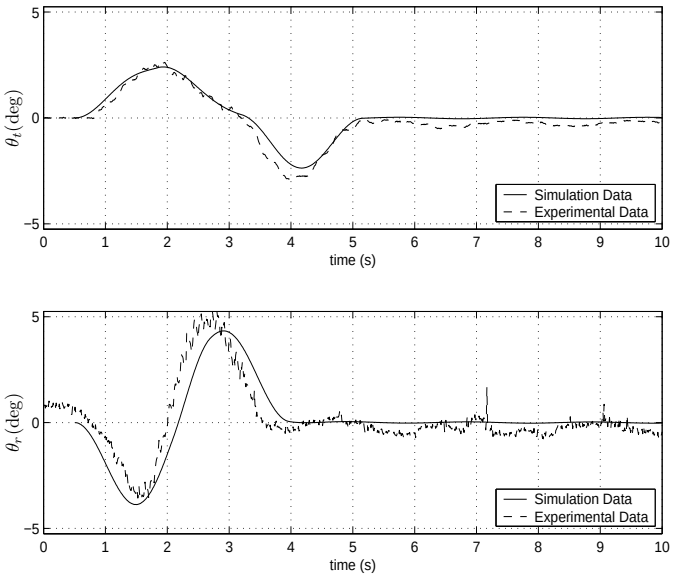

Fig. 13. Swing angles where the maneuver parameters were found using a simulation that included the actuator dynamics. Joint rates were allowed to take on any value.

three competing characteristics of a maneuver – speed, residual swing, and final position accuracy. The maneuver generation process attempted to move the payload to minimize residual swing, subject to a final time inequality constraint. This resulted in a final position error of the crane, although relatively small. The amount of final position error increases with saturation, therefore, a balance must be struck between increasing maneuver speed and final positioning accuracy. This effect is illustrated in Figure 9 where the basis function from Figure 4 is subjected to a maximum velocity of 0.4 deg/s. Future work should consider additional basis function parameterization such that this trade-off could be eliminated.

TABLE X
FINAL POSITIONS

		Slew α	Luff β
Commanded Position	[deg]	40.0	35.0
Non-saturating maneuver using ideal servo model	[deg]	39.6	33.9
Non-saturating maneuver using nonlinear servo model	[deg]	39.3	33.6
Saturating maneuver using ideal servo model	[deg]	38.0	33.6
Saturating maneuver using nonlinear servo model	[deg]	38.0	33.6

V. CONCLUSION

In previous off-line maneuver generation basis function parameters were constrained such that servo dynamics remained ideal, and that the crane inputs were symmetric. Real systems have non-linearities which make closed-form, symmetric solutions an unreasonable expectation.

Nevertheless, the results illustrated that – at least in the case where saturation is the dominant non-linearity – this traditional maneuver generation process can be used to for sufficiently slow maneuvers, but, the full capability of the crane is not realized. To solve this problem, an accurate servo dynamic model, including non-linearities, was used in the maneuver generation process. This allowed the maneuver to exploit the entire operating range of the crane, resulting in better swing suppression and faster operation.

An interesting future project would be exploring the effect parameter uncertainty has on the optimization process.

ACKNOWLEDGMENT

The authors would like to thank Sandia National Laboratories, NSWC Carterock, and the anonymous reviewers.

REFERENCES

[1] G. G. Parker, R. D. Robinett, B. J. Driessen, and C. R. Dohrmann, "Operator-in-the-loop control of rotary cranes," in *Proceedings of the 1996 International Society for Optical Engineering Symposium on the Smart Structures and Materials; Industrial and Commercial Applications of Smart Structures Technologies*, Feb. 1996, vol. 2721, pp. 364–372.

[2] Neil Singer and Seering C., "Preshaping command inputs to reduce system vibration," *Journal of Dynamic Systems, Measurement, and Control*, vol. 112, no. 1, pp. 76–82, 1990.

[3] Y. Sakawa and A. Nakazumi, "Modeling and control of a rotary crane," *Journal of Dynamic Systems, Measurement, and Control*, vol. 107, pp. 200–206, 1985.

[4] P. Vaha, S. Pieska, and E. Timonen, "Robotization of an offshore container crane," in *Proceedings of the 19th ISIR International Symposium*, 1988, pp. 637–648.

[5] J.W. Auernig and H. Troger, "Time optimal control of overhead cranes with hoisting of the load," *Automatica*, vol. 23, no. 4, pp. 437–447, 1987.

[6] J.J. Hämäläinen, A. Marttinen, L. Baharova, and J. Virkkunen, "Optimal path planning for a trolley crane: fast and smooth transfer of load," *IEE Proceedings - Control Theory Applications*, vol. 142, no. 1, pp. 51–57, 1995.

[7] M. W. Noakes and J. F. Jansen, "Generalized inputs for damped-vibration control of suspended payloads," *Robotics and Autonomous Systems*, vol. 5, no. 2-3, pp. 199–205, 1992.

[8] K. A. F. Moustafa and A. M. Ebeid, "Nonlinear modeling and control of overhead crane load sway," *Journal of Dynamic Systems, Measurement, and Control*, vol. 110, no. 3, pp. 266–271, 1998.

[9] N. Blazicevic and B. Novakovic, "Control of a rotary crane by a combined profile of speeds," *Strojarstvo*, vol. 38, no. 1, pp. 13–21, 1996.

[10] R Souissi and A.J. Koivo, "Modeling and control of a rotary crane for swing-free transport of payloads," in *The First IEE Conference on Control Applications*, 1992, pp. 782–787.
[11] B. J. Petterson and R. D. Robinett, "Model-based damping of coupled horizontal and vertical oscillations in a flexible rod," *Journal of Intelligent and Robotic Systems*, vol. 4, pp. 285–299, 1991.

Michael J. Agostini received his B.S. and M.S. degrees in mechanical engineering from Michigan Technological University where he is currently a Ph.D. candidate in mechanical engineering. Michael's research interests include non-linear control and adaptive systems.

Gordon Parker (M'95) received the B.S. degree in electrical and systems engineering from Oakland University in 1987, and the M.S. degree in aerospace engineering from the University of Michigan in 1988. He obtained the Ph.D. degree from State University of new York at Buffalo in 1994 in mechanical engineering. Between 1989 and 1996 he worked at General Dynamics, Space Systems and Sandia National Laboratories in the areas of structural dynamics and control. In 1996 he joined the Mechanical Engineering - Engineering Mechanics department of Michigan Technological University where he is an Associate Professor. His research interests include design and control of active structures, and nonlinear control spacecraft.

Hanspeter Schaub received his B.S., M.S. and Ph.D. degrees in 1992, 1994 and 1998 from Texas A&M University in College Station, Texas, all in aerospace engineering. After a one-year post-doctoral appointment at Texas A&M University working on the Techsat-21 spacecraft formation flying program, he has been an employee of ORION International Technologies working on-site at Sandia National Labs as a contract research engineer. In 2001 he also served as an adjunct professor at Michigan Technological University. He has published about 50 papers and 1 book in the field of astrodynamics and nonlinear control and is the co-owner of a patent on a relative navigation sensing system. His research interests include nonlinear dynamics and control, astrodynamics and celestial mechanics, space-based sensing systems, and in the recent years spacecraft formation flying.

Kenneth Groom received a BS and MS in Mechanical Engineering from Auburn University and a MS and PhD in Electrical Engineering from Purdue University. His honors during that time include Best Student Paper IEEE International Conference on Robotics and Automation 1997 (redundant manipulator control), Best Paper American Society of Mechanical Engineers Alabama Conference 1984 (welding with infrared sensor feedback), as well as Eta Kappa Nu, and Phi Theta Kappa honoraries. He also received two patents for shape-memory actuators.

His current interests lie in controls, sensors and robotics. For the past 5 years, he has been employed by Sandia National Laboratories as Principle Investigator on crane based ship-to-ship cargo transfers in rough seas. He has received two patents concerning controllers for shipboard cranes and has authored multiple conference papers on the subject. In November of 2002, one such controller was successfully demonstrated on a 600 ft naval vessel in sea-state three conditions.

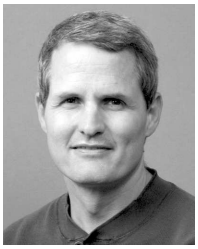

Rush Robinett III has degrees in Aerospace Engineering from Texas A&M University (B.S. - 1982, Ph.D. - 1987) and The University of Texas at Austin (M.S. - 1984). He has authored over 90 technical articles and publications including a book and holds 4 patents as well as 4 more patents pending. Rush began his career at Sandia National Laboratories in 1988 as a Member of the Technical Staff working on the Ballistic Missile Defense program. In 1995, he was promoted to Distinguished Member of the Technical Staff. In 1996, Rush was promoted to technical manager of the Intelligent Systems Sensors and Controls Department within the Robotics Center at Sandia where he and his staff developed a new area of robotics called Engineered Collectives. In 2002, Rush was promoted to Deputy Director of the Energy and Transportation Security Center where, presently, he is developing new opportunities in distributed, decentralized power and transportation infrastructures.